Type of paper: full length article - revision (*Computers and Geotechnics*)
Date text written: March 2020
Date of revision: June 2020
Number of words in main text = 6463
Number of figures = 15
Number of tables = 2

Network analysis of heat transfer in sands

Author 1
Wenbin Fei, PhD student, ME, BE
Department of Infrastructure Engineering, The University of Melbourne, Parkville, Australia
ORCID: 0000-0002-9275-8403

Author 2
Guillermo A. Narsilio✉, PhD, MSc (Math), MSc (CE), CEng
Department of Infrastructure Engineering, The University of Melbourne, Parkville, Australia
ORCID: 0000-0003-1219-5661

Full contact details of corresponding author
Guillermo A. Narsilio, Deputy Head (Research) and Associate Professor
Engineering Block B 208, Department of Infrastructure Engineering, The University of Melbourne, Parkville, VIC 3010, Australia
Email: narsilio@unimelb.edu.au, Phone: +61 (3) 8344 4659, Fax: +61 (3) 8344 4616

Abstract

Differences in the effective thermal conductivity (ETC) between measurements and models may be attributed to the limited ability to capture microstructural information of geomaterials. Today, computed tomography (CT) technology offers unprecedented access to such information, particularly for sands. Since a sand can be represented as a contact network made of nodes (particles) connected by edges (contacts), features (or variables) arising from the contact network can characterise particle connectivity. However, existing contact network features neglect the contribution of contact quality and of small gaps between neighbouring particles to heat transfer. To redress these issues, this paper introduces new weighted *contact* network features by considering contact area at each edge in the *contact* network. Additionally, *thermal* network features are proposed by considering small gaps as edges with/without being weighted by thermal conductance. All network features are calculated based on CT images of five real sands. The relationships between each feature and ETC are investigated. The results show that some network features that account for both the particle connectivity and contact quality can be used to predict ETC accurately. Advantages and limitations of this approach are also identified.

Keywords: fabric/structure of soils; particle-scale behaviour; sands; finite-element modelling; complex network theory;

1. Introduction

Heat transfer processes in soils are important in a variety of engineering applications. Take shallow geothermal energy projects as an example. Here heat is exchanged between the ground and fluid circulating in pipes embedded directly in the soil [1] (or rock) in purposely built boreholes or trenches, or incorporated in geostructures (e.g., energy piles, energy walls) [2]. With the help of a heat pump, the heat is upgraded to efficiently provide space heating and cooling to buildings. The effective thermal conductivity (ETC) of the ground is a key parameter in geothermal design [3]. ETC presents the ease of heat transfer in the ground, and thus largely determines the efficiency of the geothermal system [4, 5].

Predicting ETC accurately is difficult due to the complex microstructure of the soils [6]. Since heat is transferred via particles [7], and porosity indicates the fraction of particles in a soil mass, the porosity is widely used to predict ETC, as it is readily obtainable. However, porosity-dependent models neglect the effects of the microstructure such as particle connectivity and contact quality on heat transfer [8-10], given that porosity is a macro-scale parameter. As a result, porosity-dependent models are rarely valid for wide porosity ranges [10], especially for materials with a large ratio of solid to fluid thermal conductivity [11].

Packing structure models offer alternatives to porosity-dependent models by using structural characteristics instead of porosity as the key controlling variable [12]. The lack of accountability of structural data may result in the difference of ETC between models and experimental methods [6]. Some scholars have proposed microstructural characteristics such as: i) the minimum gap between particles and the mean local curvature [13, 14], ii) connectivity represented by Voronoi tessellation [15, 16], iii) an order characteristic by measuring rotational symmetry of particles [14], iv) the ratio between the radius of contact area and particle radius [17], v) particle size distribution [18], and vi) some results for typical regular structures [19] (simple cubic, body-centred cubic and face-centred cubic). However, these works focus on sphere packings rather than the irregular sand-size particles prevalent in nature. Even though a number of microstructural descriptors are available in the literature [20], the characterisations of particle connectivity in real sands are still scarce.

Recently, the wider availability of X-ray computed tomography (CT) has shed light on the microstructure of irregular granular materials [21-23]. Using imaging techniques, the structures of granular materials can be simplified into networks [24, 25]. A network is a web consisting of nodes and edges, which are defined depending on the type of network. For instance, in a *contact* network, each node represents a particle in a sand, and an edge is created when two particles touch. Based on the network, a number of network features (or variables such as degree, walks, paths, cycles, centralities and clustering coefficients in the literature [26]) can be calculated using complex network theory, and be employed to characterise the microstructure of granular materials. Russel et al. [27] advocated that a *contact* network could be used to understand mechanical stability, and a *pore* network could offer knowledge about the flow pathway in deforming granular materials. Fei et al. [28] found the local clustering coefficient (a contact network feature presenting particle connectivity) together with particle shape descriptor [29] have good correlations with ETC of sands under loadings. However, their work only applied a few *contact* network features to quantify the particle connectivity without evaluating the interparticle contact quality. Furthermore, the *contact* network features could not characterise the contribution of small gaps (near-contacts) between neighbouring particles to ETC. Since particle connectivity variables are still scarce, a question raised is whether more particle connectivity parameters can be discovered and whether a single variable can cover both particle connectivity and contact quality. Fei et al. [30] constructed *contact* networks and also extended them to *thermal* networks by considering the small gaps between neighbouring particles as new edges. Analytical ("exact") expressions can be used to compute the interparticle contact area and construct networks for sphere packings; however, different image processing techniques and mathematical approaches are required when dealing with real sands.

In the present paper, five irregular sands were used to quantify the correlations between network features and ETC. Both *contact* network features and *thermal* network features were extracted from each irregular sand. They are not only used to characterise the particle connectivity but also contact quality by considering the contact area in *contact* networks or thermal conductance in *thermal* networks, resulting in comprehensive microstructural parameters. Then, machine learning techniques were employed to evaluate the importance of the microstructural parameters in predicting ETC.

2. Materials

Five sands with different particle shapes were selected, as shown in Fig. 1. The glass beads are round and made of silica, enabling studying almost perfectly regular packings, a strategy and material often adopted by many geotechnical researchers [31-33]. The particles of the Ottawa 20-30 sand [34] also contain quartz [35] and are rounded over time by hydromechanical weathering (e.g., in a river). Angular sand is also mainly composed of quartz, but its particles are more irregular than those of Ottawa sand. The particles in crushed Schist A are more irregular still, and are mostly made of chlorites. Finally, Schist B is collected from the Delamarian Fold Belt in western Victoria, Australia, and consists of quartz and biotite; its particles are the most irregular of the group under study, with half of them being elongated and platy [36]. The measured particle sizes of the five sands are summarised in Table 1.

<Fig. 1 around here>

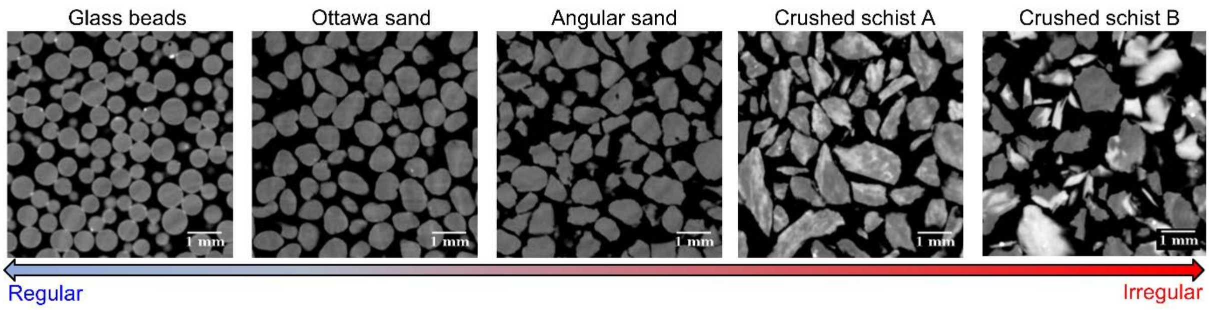

Fig. 1. Five types of natural sand scanned with computed tomography.

<Table 1 around here>

Table 1 Particle size for the selected sands

Sand	D_{50} (mm)	Min particle diam. (mm)	Max particle diam. (mm)
Glass beads	0.60	0.50	0.70
Ottawa sand	0.73	0.60	0.85
Angular sand	0.89	0.60	1.18
Crushed schist rock A	0.84	0.50	1.18
Crushed schist rock B	0.84	0.50	1.18

3. Methods

Fig. 2 shows a proposed framework which includes six blocks. In block 1, image stacks with a certain interval (resolution) were created by air-pluviating the sand in a PVC cylinder with a diameter of 25 mm and a height of 25 mm, and then scanning it with X-ray CT. The image stacks were cropped to the representative element volume and then used for three purposes: (i) calculating classic geotechnical microstructural parameters such as the average particle diameter and contact area ; (ii) constructing networks and computing network features (block 2); (iii) simulating heat transfer and calculating ETC using finite element method (FEM) (block 3); and For each feature, its correlation coefficient against ETC was presented using six mathematical models (block 5). The model with the highest correlation coefficient was recognised as the 'best fit' model, and the correlation coefficient was used to assess the importance of the feature in predicting ETC (block 6).

<Fig. 2 around here>

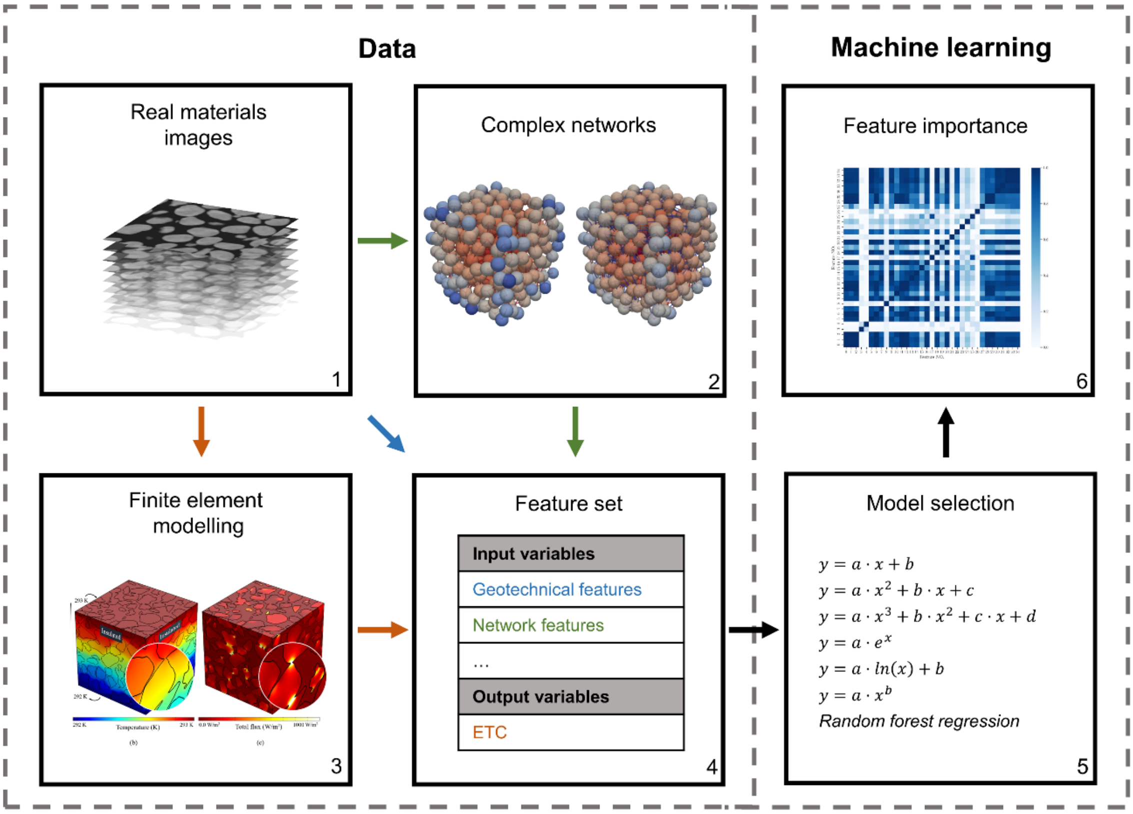

Fig. 2 Framework used to calculate the microstructural parameters and analyse their impact on the effective thermal conductivity of granular materials.

3.1 Numerical simulation and experiment

Since this paper focuses on the impact of microstructure on ETC, the variance in ETC induced by mineral components was assumed to be mitigated by assigning the same thermal conductivity to the solids in the finite element models. The numerical results were also validated using the experimental results.

3.1.1 Finite element simulation

For each sand, four representative element volumes (REVs) of dimensions 4.55 × 4.55 × 4.55 mm (320 grains in Ottawa sand as an example) were randomly selected from the CT images. These dimensions are consistent or exceeding previously reported REVs of similar materials [37-40]. As shown in Fig. 3, the geometry of each subsample was reconstructed based on these CT images. The solid and pore phases were then split using the widely accepted Otsu threshold segmentation [41-44]. The thermal conductivity of the solid used in this paper was 3 $\mathrm{W/(m\ K)}$ [45-47], while that of air in the pore spaces was taken as 0.025 $\mathrm{W/(m\ K)}$ [48]. Reconstruction and segmentation were completed using Simpleware ScanIP [49] with a further meshing step. The mesh was then imported to a FEM software application called COMSOL Multiphysics [50] to simulate heat transfer [29, 51].

In COMSOL Multiphysics, the boundary temperature at the top T_a was prescribed as 293 K, while that on the bottom T_b was 292 K to create a thermal gradient to drive heat flux (a different thermal gradient would render similar results), and the other boundary surfaces were insulated (i.e., nil heat flux). Next, the temperature distribution was computed by solving the governing energy balance equations [52]. Since dry sands were tested using a thermal needle, the simulation model only considered heat conduction. Fourier's law was used to calculate the conductive heat flux, and a continuity equation was applied to ensure flux continuity at the particle-pore interface [51]. An example of the temperature and flux distribution is shown in Fig. 3. Based on the solutions for the heat flux at the top (inlet) and bottom (outlet) boundaries, the ETC at the two surfaces was calculated using Equation 1. The mean ETC at the two boundaries was regarded as the ETC of the whole sample:

$$\lambda_{eff} = \frac{\frac{1}{A}\int_A Q_z \, dA}{\frac{T_a - T_b}{L}} \tag{1}$$

where λ_{eff} (W/mK) is the ETC of the sample, A (m^2) is a typical cross-sectional area, L (m) is the height of the packing, T_a = 293 K and T_b = 292 K are boundary temperatures at the top and bottom of the sample respectively, and Q_z (W/m^2) is the vertical heat flux at a typical cross-section.

<Fig. 3 around here>

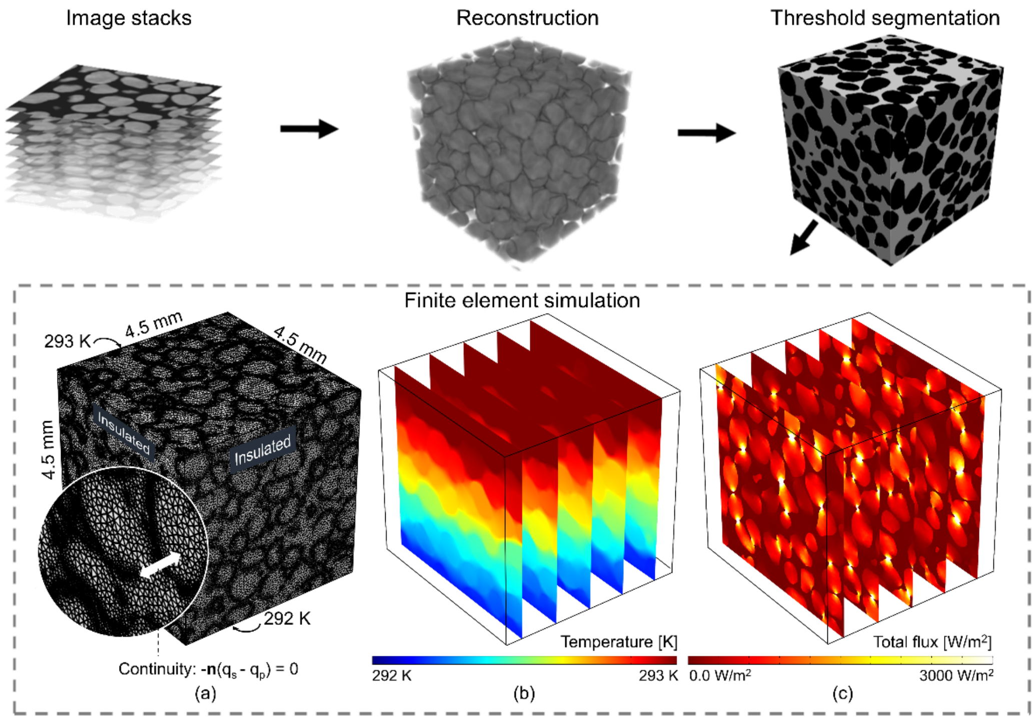

Fig. 3 The process of heat transfer simulation based on CT scanned images.

3.1.2 Laboratory experiment

In order to validate the ETC from numerical simulation, thermal needle testings were conducted to measure the ETC. The sands were rained into a PVC cylinder of diameter 50 mm and height 120 mm using the same air-pluviation method to prepare a homogeneous specimen. A 100-mm long thermal needle probe of diameter 2.4 mm was used to measure the ETC at room temperature, following ASTM standard D5334-14 [53]. The diameter of the selected needle was larger than the particle diameter (Table 1) to ensure more contacts between the probe and particles. A KD2 Pro thermal properties analyser with a manufacturer reported accuracy of $\pm 10\%$ for 0.2-4 W/mK materials was used [54]. This is consistent with standard requirements.

3.2 Complex networks

3.2.1 Network construction

A *contact* network can be constructed by assigning a node to the centroid of each particle and generating an edge between two nodes if the corresponding particles touch (Fig. 4). The particles in the CT images (Fig. 1) were connected, and watershed segmentation was required to split the connected particles into individual ones using an add-in called 'MorphoLibj' [55] in Fiji [56]. To avoid over-segmentation of the contact area, which is important for heat transfer [7], a six-voxel neighbourhood [57] was used in the watershed algorithm. However, the contact network only considered interparticle heat transfer and neglected heat conducts via the air in the small gap between particles [46]. To address this, the *contact* network was extended to a *thermal* network by considering the small gaps as 'near-contacts' and allocating edges to them, as shown in Fig. 4.

<Fig. 4 around here>

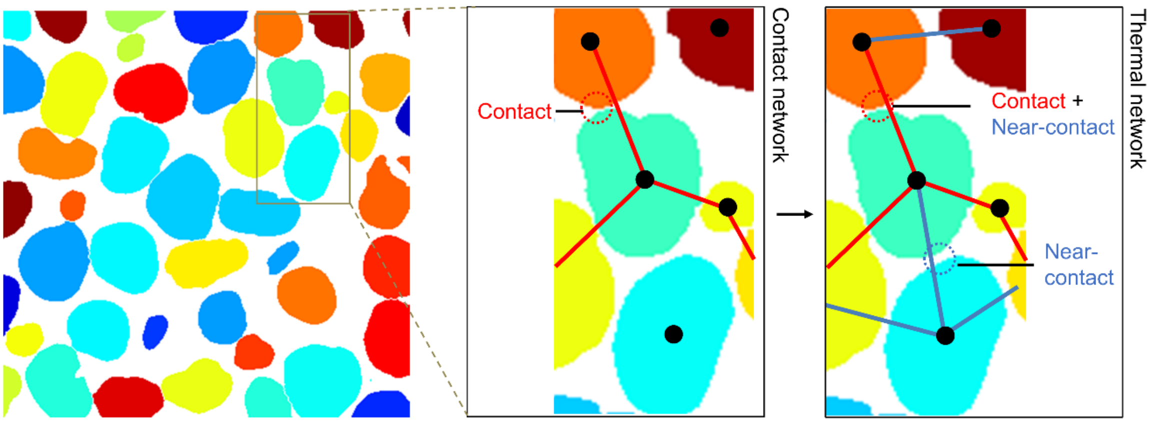

Fig. 4 The heat transfer path includes both interparticle contact and the small gaps between particles. Only interparticle contact is considered in the *contact* network, while both paths are involved in the *thermal* network.

In a sphere packing (Fig. 5 (a)), any two adjacent particles are connected by either a circular contact of radius r_c or a gap of distance h_{ij}. Hence, the network edges related to interparticle contacts and near-contacts can be easily determined using analytical expressions. In contrast, the irregular particle shape of natural sands obtained through micro-CT (Fig. 5 (b)) posts a significant challenge to build networks representing them. In this work, the boundary voxels of each particle were first identified in the watershed-segmented CT images using an edge detection algorithm and used to determine the interparticle contacts and near-contacts as follows: Boundary voxels shared between two particles made up an interparticle *contact*. For those voxels that are not in contact, if the distance between two voxels at the boundaries of two neighbouring particles are less than a certain threshold distance, they were labelled as in a *near-contact*. By following the work of van der Linden et al. [58] and Fei et al. [28], half the average particle radius was selected as this threshold distance by calibrating our thermal network model with network models for sphere packings [46] which was developed based on theoretical equations. There is another important difference when dealing with sphere packings vs real sands. To compute the thermal conductance at interparticle contacts and near-contacts, the analytical solutions are available for sphere packings [46]. In contrast, the thermal conductance at the interparticle contact in real sands is computed in this work using the number of shared boundary voxels (Fig. 5 (b)), and the thermal conductance at near-contacts is calculated using the distance between voxels and computing conductance in parallel of a series of cylinders filling the near-contact gap between particles [28].

< Fig. 5 around here>

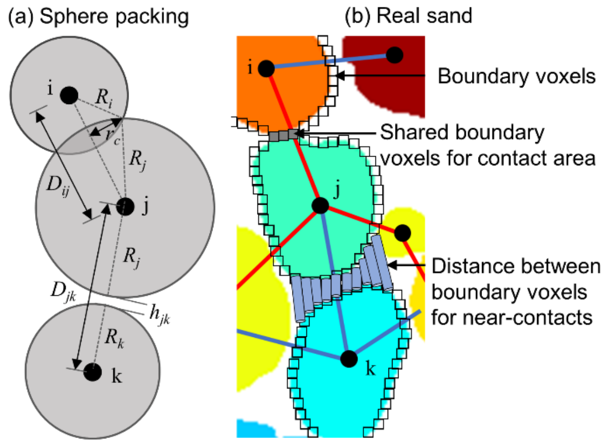

Fig. 5 Identification of the interparticle contact and the near-contact in (a) a sphere packing and (b) a real sand from voxelated images.

3.2.2 Network features

After constructing the networks, network features can be extracted by using complex network theory. Four types of features were used here: (i) *centrality*; (ii) *network scale*; (iii) *cycles*; and (iv) *clustering*.

Centrality quantifies the 'significance' of a node, edge or structure in a network [59]. As shown in Fig. 6 (a), five metrics of centrality are used in this work. They highlight the significance of the nodes in different ways. The *degree* $\kappa(i)$ of a node *i*, also known as the *coordination number,* is the number of edges linked to this node. *Closeness centrality* quantifies the closeness of a node to others in a network, and high *closeness centrality* means a node is in a 'central' position. *Betweenness centrality* qualifies the importance of a node or edge that acts as a 'bridge' between other nodes or edges. A high *betweenness centrality* indicates that the node or edge plays a vital role in the heat transfer path. *Eigenvector centrality* measures the wide-reaching influence of a node in a network by assigning a relative score to each node. A node with high *eigenvector centrality* indicates that it has good connections to other nodes with high scores. *Top-to-bottom edge betweenness centrality* is used to only consider the corresponding heat transfer paths when heat travels predominantly in one dimension (say, top to bottom) in response to the thermal gradient prescribed in this direction. Let us summarise next the formal definitions of key network features.

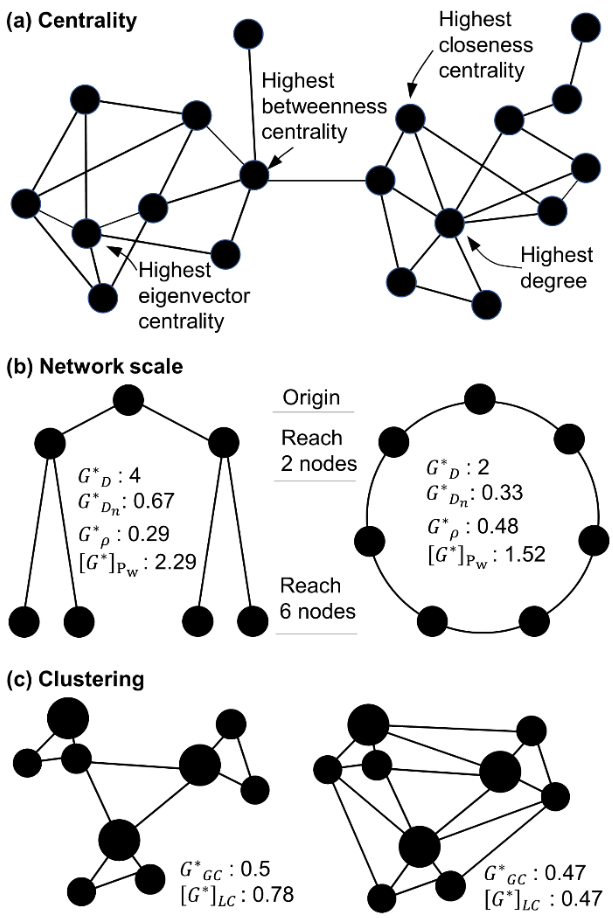

Fig. 6 Network features: (a) Identifying the nodes with the highest values of the different types of centrality features in a given network, (b) network scale features and (c) clustering coefficients for different networks with the same number of nodes [30].

For a node *i* in a node-set *V*, its closeness centrality is defined as the reciprocal of the sum over the shortest path *d(i,j)* from the node *i* to all other nodes *j* (Equation 2) [60].

$$[G^*]_C(i) = \beta \left[\sum_{j=1}^{|V|-1} d(i,j) \right]^{-1} \tag{2}$$

where β is a normalisation term set to be the number of reachable nodes $|V| - 1$ and the number of maximum possible edges $(|V|(|V| - 1))/2$ in this study (both normalisations are trialled), here |*V*| is the number of nodes in the network.

As shown in Equation 3, the *node betweenness centrality* of node *i* can be calculated as the sum of the ratio of $\sigma(j,k|i)$ (the number of shortest paths from any other two nodes *j* and *k* and pass *i*) to $\sigma(j,k)$ (the number of shortest paths from any other two nodes *j* and *k*). Similarly, the *edge betweenness centrality* of edge *e* is computed as the ratio of $\sigma(j,k|e)$ (the number of shortest paths from any other two edges *j* and *k* and pass *e*) to $\sigma(j,k)$ (the number of shortest paths from any other two edges *j* and *k*). The *betweenness centrality* can be further normalised with β, which is 2*/(*|*V-1*|*(*|*V*|*-2))* for *node betweenness centrality* and *2/[*|*V*|*(*|*V*|*-1)]* for *edge betweenness centrality* [61].

$$[G^*]_{B^{node}}(i) = \beta \sum_{j,k \epsilon V} \frac{\sigma(j,k|i)}{\sigma(j,k)} \tag{3}$$

Network scale indicates the average distance from one node to others in a network. It helps in understanding the speed of heat transfer through networks with different topologies. As shown in Fig. 6 (b), , heat transfers faster in a 'tree' network, since only two steps are required to reach six nodes compared with the three steps required in a 'ring' network. The *network diameter* G_D^*, *average shortest path length* $[G^*]_{P_W}$ and *network density* G_ρ^* are used here to quantify the network scale. *Network diameter* is the length of the longest of the shortest paths in a network, and the *normalised network diameter* $G_{D_n}^*$

can be achieved by dividing G_D^* by |*V*|-*1*. As heat is transferred from the top surface (inlet) to the bottom surface (outlet) in the FEM models, as shown in Fig. 3, the *average shortest path length between the inlet and outlet nodes* is related to the heat transfer path and is used as another network feature. *Network density* G_ρ^* is the ratio between the real edge number and the potential edge number, and represents the different particle connectivity in networks. The values of network-scale-type features in ring and tree networks are shown in Fig. 6 (b).

A *cycle* is a loop that begins and ends at the same node. A *L-cycle* indicates that a loop has *l* edge, meaning that a *3-cycle* is a triangle. As triangles are isostatic [62-64], a *3-cycle* resists deformation, and the number of *3-cycles* represents the rigidity of the microstructure of a sample [28, 65]. In this work, the number of *3-cycles* and the normalised value based on edge and node numbers were calculated.

Clustering measures the integrity of a network. The left figure of Fig. 6 (c) shows a fractured network with three clusters, where only one edge connects each of the clusters. In contrast, the right figure of Fig. 6 (c) shows a relatively integrated network, where the three clusters are well connected. The global [66] and local cluster coefficients [67] can be used to quantify the clustering of networks, as defined in Equations 4 and 5, respectively. It can be seen from Fig. 6 (c) that a fractured network has a higher clustering coefficient than an integrated network.

$$G^*{}_{GC} = 3\,\frac{number\ of\ triangles}{number\ of\ connected\ triples} \tag{4}$$

$$[G^*]_{LC}\,(\mathrm{i}) = \frac{2T(i)}{\kappa(i)[\kappa(i)-1]} \tag{5}$$

where *T(i)* is the number of triangles pass node *i* and $\kappa(i)$ is the degree of node i.

Network features were determined from the contact and thermal networks for each sample. An edge represents an interparticle contact in a contact network (Fig. 4) and the contact area can be calculated using the shared boundary voxels. As a larger contact area leads to greater heat transfer via interparticle contact [68, 69] and a larger *degree* indicates more interparticle contacts, the length of each edge for the degree was weighted by the contact area in the contact network which only considered interparticle contact. Hence, the physical meaning of $G_{\kappa_w}^C(i)$ of node i is the total contact area between node i and its neighbours, $[G^C]_{\kappa_w}$ is the average of $G^C_{\kappa_w}$ of all nodes in a network. As other network features with higher value such as closeness centrality in Equation 2 could be achieved by minimising the length of the shortest path, the length of each edge for other contact network features was weighted by the reciprocal of the contact area. Similarly, since thermal conductance can be calculated at interparticle contacts and near-contacts at thermal network edges, the length of each edge for *degree* was weighted by sum of thermal conductance through interparticle contact and near-contact between two neighbouring particles. Consequently, the physical meaning of $G^T_{\kappa_w}(i)$ of node i is the total thermal conductance between node i and its neighbours, $[G^T]_{\kappa_w}$ is the average of $G^T_{\kappa_w}$ of all nodes in a network. The length of each edge for other thermal network features can be weighted by the reciprocal of thermal conductance.

Classic geotechnical parameters including porosity and contact radius ratio (the radius of the contact area divided by that of the particle) were also calculated for each sample. Finally, all features were collected as a feature set (Table 2). The features were scaled (normalisation terminology in machine learning) [30]. since they had distinct ranges.

<Table 2 around here>

Table 2 Summary of features used in this work

Type	No.	Notation	Attribute
Geotechnics	1	n	Porosity
	2	γ	Contact radius ratio
	3	D_{50}	Average particle diameter
	4	C_u	Coefficient of uniformity
	5	C_c	Coefficient of curvature
Centrality	6	$[G^*]_\kappa$	Degree ('coordination number' in a contact network)
	7	$[G^*]_{\kappa_w}$	Weighted degree
	8	$[G^*]_C$	Closeness centrality
	9	$[G^*]_{C_{n1}}$	Closeness centrality normalised by $\lvert V\rvert - 1$
	10	$[G^*]_{C_{n2}}$	Closeness centrality normalised by $[\lvert V\rvert(\lvert V\rvert - 1)]/2$
	11	$[G^*]_{C_w}$	Weighted closeness centrality
	12	$[G^*]_{C_{nw1}}$	Weighted closeness centrality normalised by $\lvert V\rvert - 1$
	13	$[G^*]_{C_{nw2}}$	Weighted closeness centrality normalised by $[\lvert V\rvert(\lvert V\rvert - 1)]/2$
	14	$[G^*]_{B^{node}}$	Node betweenness centrality
	15	$[G^*]_{B^{node}_n}$	Normalised node betweenness centrality
	16	$[G^*]_{B^{node}_w}$	Weighted node betweenness centrality
	17	$[G^*]_{B^{node}_{nw}}$	Normalised weighted node betweenness centrality
	18	$[G^*]_{B^{edge}}$	Edge betweenness centrality
	19	$[G^*]_{B^{edge}_n}$	Normalised edge betweenness centrality
	20	$[G^*]_{B^{edge}_w}$	Weighted edge betweenness centrality

Type	No.	Notation	Attribute
	21	$[G^*]_{B_{nw}^{edge}}$	Normalised weighted edge betweenness centrality
	22	$[G^*]_{B_{w}^{edge^{tp}}}$	Weighted top-to-bottom edge betweenness centrality average
	23	$[G^*]_{B_{nw}^{edge^{tp}}}$	Normalised weighted top-to-bottom edge betweenness centrality average
	24	$[G^*]_E$	Eigenvector centrality
	25	$[G^*]_{E_w}$	Weighted eigenvector centrality
Network scale	26	G^*_ρ	Network density
	27	G^*_D	Network diameter
	28	$G^*_{D_n}$	Normalised network diameter
	29	$[G^*]_{P_w}$	Weighted shortest path (average)
	30	$[G^*]_{P_w^{tp}}$	Average weighted shortest path between inlet and outlet nodes
Clustering	31	${G^*}_{GC}$	Global clustering coefficient
	32	$[G^*]_{LC}$	Local clustering coefficient
Cycles	33	G^*_{3C}	Number of 3-cycles
	34	$[G^*]_{3C^{node}}$	Average number of node 3-cycles
	35	$[G^*]_{3C^{\mathrm{edge}}}$	Average number of edge 3-cycles

$[G^*]$ is a unified characteristic, and *$[G^C]$* refers to *contact* network features, while *$[G^T]$* refers to *thermal* networks. The brackets in *[G*]* indicate an average value of the parameter. $|V|$ is the total number of nodes in the network.

3.3 Model selection and feature importance

3.3.1 Model selection

We aimed to identify the essential features for ETC from the 35 features shown in Table 2. For each pair of a feature and ETC, six common mathematical models (linear, quadratic polynomial, cubic polynomial, exponential, logarithmic and power) were used to compute their correlation coefficient R^2. These six models were linearized for higher computational efficiency. Among the six models, the one with the highest R^2 was selected as the 'best fit' model. The challenge when using different orders of polynomials was to avoid over-fitting. To address this concern, LASSO regression and cross-validation were used in this study [70].

LASSO (least absolute shrinkage and selection operator) regression [71] is an extension of regression analysis that considers regularisation in generalised linear models. It penalises the non-zero coefficient of the variables in linear models, meaning that many coefficients will be zeroed. The process of zeroing covariates is also a variable selection which benefits the interpretability of the models and the accuracy of prediction. We adopted the LASSO regression, embedded in a Python library called scikit-learn [72].

In a prediction problem, one part of the dataset (training dataset) is used to train the model, while another part (validation or testing dataset) is used to test its performance. However, if the dataset is small, there may be insufficient unknown data for testing. K-fold cross validation [73] can resolve this issue by partitioning the dataset randomly into K subsets, each of which is used in turn as a validation dataset, while the other K−1 subsets are combined as the training dataset, generating a total of K scores for R^2. The average K score is then used to evaluate the fitting accuracy of the model. As six models were involved in this work, the model with the highest average score was selected as the 'best fit' model. K was set to four in this work.

3.3.2 Feature relevance

The average score can only be used to evaluate the model, rather than to assess the importance of a feature, since the type of model is a new feature that is not considered in training. In order to evaluate the importance of each score to the ETC, a new general correlation coefficient R^2 was calculated, based on all of the data.

4. Results and Discussion

4.1 Effective thermal conductivity

Four subsamples were selected from each sand, and ETC values were computed using FEM, as shown in Fig. 7. The simulated results were also validated using the experimental results and data reported by Narsilio et al. [51] and Yun and Santamarina [7]. The simulated ETC decreases as porosity increases from 0.35 to 0.50. Increasing porosity indicates a lower percentage of solid particles in the sand, resulting in a potential decrease in interparticle contact number, which forms the primary heat transfer path in dry granular materials [45]. However, when the porosity increases beyond 0.50, the variation in the ETC becomes minimal. This demonstrates that the porosity is not directly related to ETC in geomaterials such as frozen ground where void space is largely occupied by ice or ice lenses, and a large porosity of more than 0.5 is common.

The experimental results show a similar trend, although their absolute values are lower. This difference arises from several aspects: (i) the error in needle probe testing; (ii) since the CT images are voxelated and the interface between the solid and void phases has a sawtooth pattern, the contact area may be overestimated when threshold segmentation is used [28, 44]; (iii) the image resolution and finite element meshing techniques cannot capture the particle surface roughness [51]. CT images with higher resolution can improve the calculation of the contact area. However, the selection of the image resolution is a trade-off between sample size and resolution: a larger sample (more grains) with lower resolution while smaller sample (fewer grains) boosting higher resolution. Estimating ETC accurately and directly from large size and high-resolution CT images using finite element methods is not currently practical.

<Fig. 7 around here>

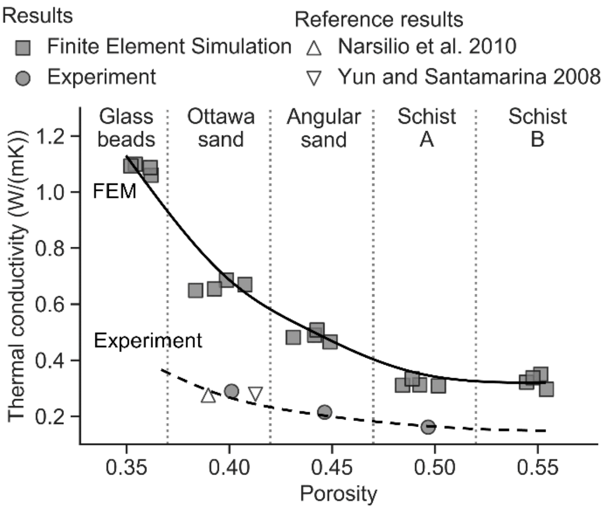

Fig. 7. The ETC of five types of sand are computed using the finite element method and validated using experimental results.

4.2 Effects of network features on ETC

Contact and thermal networks were constructed to compute the network feature set in Table 2. Fig. 8 shows examples of these networks for the same sample. The thermal network has more edges than the contact network does since it considers not only interparticle contacts but also near-contacts. The different number of edges changes the values of the network features. As ‘near-contact’ edges in the thermal network reduce the shortest path between nodes, the node closeness centrality calculated from the thermal network is larger than that for the contact network, according to Equation 2.

<Fig. 8 around here>

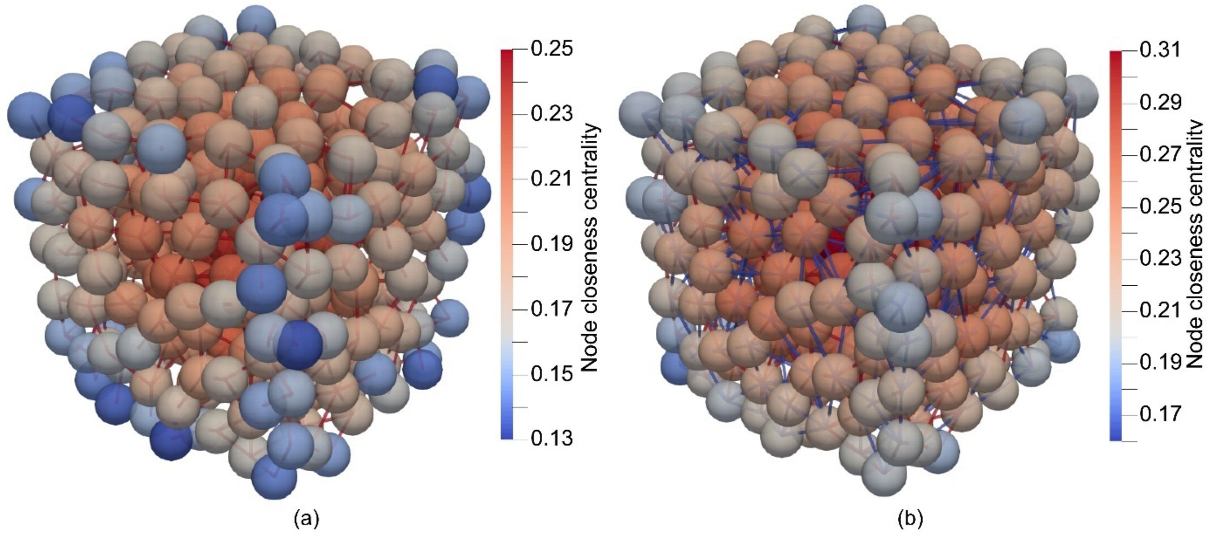

Fig. 8. Contact and thermal networks: (a) Only real contacts (red edges) are considered in a contact network, while (b) both real contacts and 'near-contacts' (blue edges) are considered in a thermal network for the same sample. Sand grains were presented by spheres with equivalent particle diameters.

Using the model selection and feature importance evaluation methods, the correlations between each pair of features and simulated ETC is calculated, and the scores are shown in Fig. 9. The 'best fit' model for each feature and the exact values of the scores are summarised in Appendix 1. Fig. 9 shows that porosity (Feature 1) as a classic geotechnical feature that has a high score of 0.93. The degree $[G^C]_\kappa$ (Feature 6) of the contact network, also known as the coordination number in geotechnics, has a high score of 0.96. Fig. 10(a) shows that ETC increases with $[G^C]_\kappa$, indicating that more interparticle contacts result in a larger ETC. Although the values of $[G^C]_\kappa$ for crushed Schist A and B are similar as shown in Fig. 10(a), the values of the four subsamples in a given sand disperses. Samples of Ottawa and angular sand may have the same $[G^C]_\kappa$ but quite different values of ETC. In contrast, the weighted degree $[G^C]_{\kappa_w}$ (Feature 7) considers the interparticle contact area at each network edge based on $[G^C]_\kappa$ (coordination number) which characterises only the particle connectivity. In other words, the physical meaning of $G^C_{\kappa_w}(i)$ of node *i* is the total contact area between node *i* and its neighbours, $[G^C]_{\kappa_w}$ is the average of $G^C_{\kappa_w}$ of all nodes in a network. Fig. 10(b) shows that $[G^C]_{\kappa_w}$ classifies the five materials into different groups, indicating a feature including both particle connectivity and contact quality (interparticle contact area) could have a better correlation with ETC. It also can be seen from Fig. 10(b) that the data for crushed Schist B do not fall on the fitted line, due to its larger contact ratio (Fig. 10(c)) than crushed Schist A, even though they have similar coordination numbers (Fig. 10(a)). The larger interparticle contact area may be because half of the particles in crushed Schist B are elongated and platy (Fig. 1) [29]. Although the score of $[G^C]_{\kappa_w}$ is slightly lower than $[G^C]_{\kappa}$ due to data deviation in crushed Schist B, weighted degree $[G^C]_{\kappa_w}$ is still a good candidate for predicting ETC, since it has a high correlation with ETC and it involves information on both particle connectivity and contact quality. Instead of quantifying the contact quality using the interparticle contact area, thermal conductance can measure both the interparticle contact quality and near-contact (Fig. 4) quality. The weighted degree $[G^T]_{\kappa_w}$ derived from the thermal network (as opposed to from the contact network, note the T superscript) was calculated by adding the thermal conductance at each thermal network edge. The physical meaning of $G^T_{\kappa_w}(i)$ of node *i* is the total thermal conductance between node *i* and its neighbours, $[G^T]_{\kappa_w}$ is the average of $G^T_{\kappa_w}$ of all nodes in a network. A curve presented by Equation 6 describes the correlation between $[G^T]_{\kappa_w}$ and ETC as shown in Fig. 10(d). The data for crushed Schist B now is on the fitted curve rather than off the fitted curve as shown in Fig. 10(b). Compared with the differences in porosity between crushed Schist A and B for the same ETC (Fig. 7), the values of $[G^T]_{\kappa_w}$ are similar, the plateau in Fig. 7 indicates that heat transfer more directly relies on the particle connectivity than the solid/pore fraction.

<Fig. 9 around here>

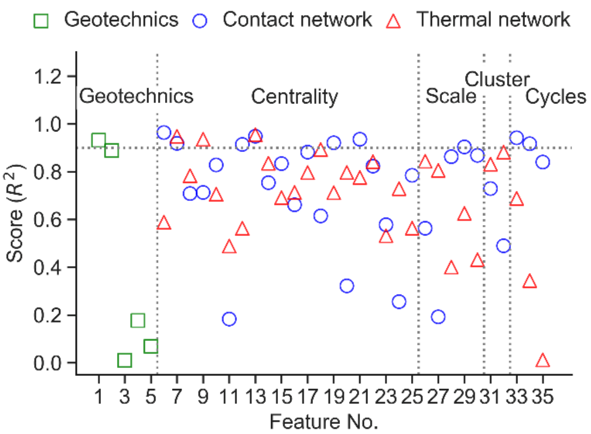

Fig. 9. The importance of each feature to ETC (feature number refers to the listing in Table 2).

<Fig. 10 around here>

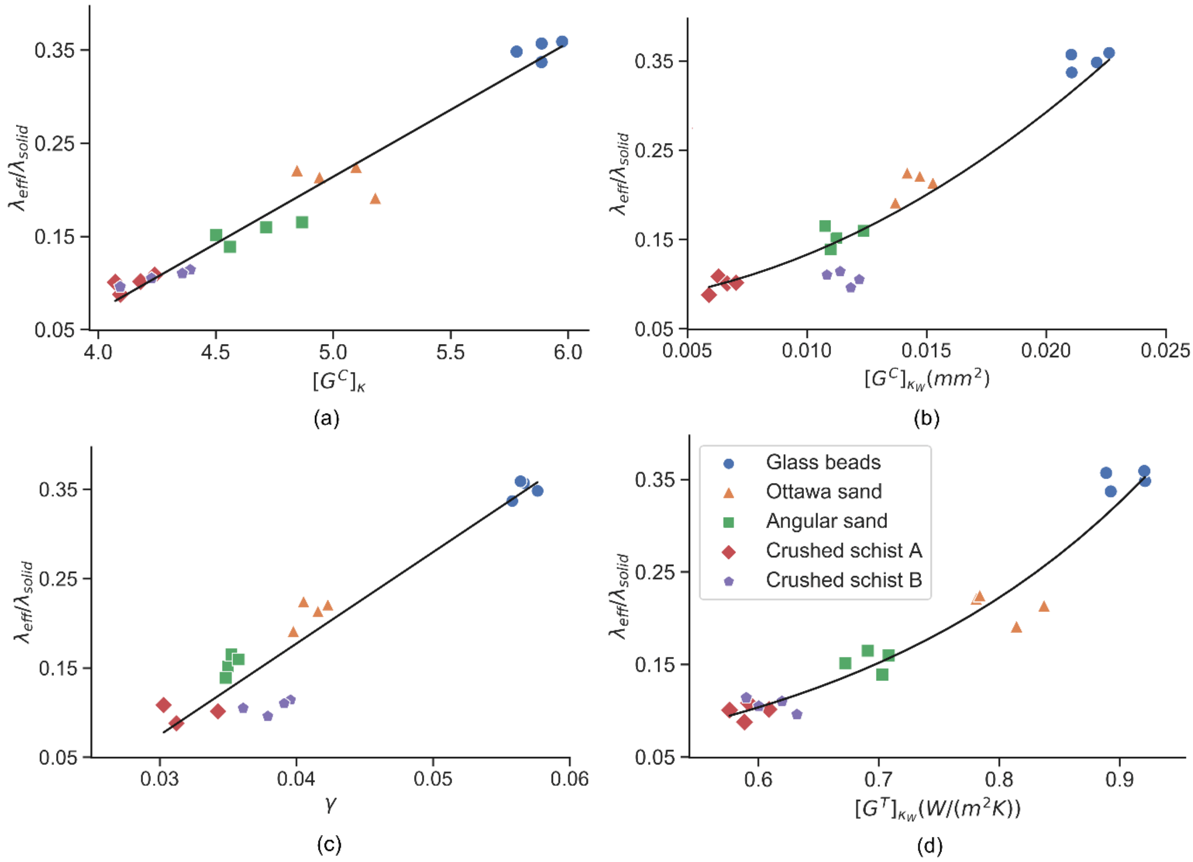

Fig. 10. Relationship between ETC and (a) contact network feature *degree* $[G^C]_\kappa$ (coordination number); (b) contact network feature *weighted degree* $[G^C]_{\kappa_w}$; (c) : *contact radius ratio* γ; and (d) thermal network feature *weighted degree* $[G^T]_{\kappa_w}$.

$$\frac{\lambda_{eff}}{\lambda_{solid}} = 1.71\left([G^T]_{\kappa_w}\right)^2 - 1.81[G^T]_{\kappa_w} + 0.58 \qquad (6)$$

For *closeness centrality* type of features (Features 8–13 in Fig. 9) which indicate the distance between nodes in a network, $[G^T]_{C_{n1}}$ (Feature 9) has the highest score of 0.94. Fig. 11(a) shows that ETC decreases with increasing $[G^T]_{C_{n1}}$; the trend is different from the relationship between ETC and other unweighted particle connectivity variables such as $[G^C]_\kappa$ for the contact network. The decreasing trend of ETC with $[G^T]_{C_{n1}}$ is because near-contacts in the thermal network reduce the shortest path *d(i,j)* used in Equation 2. The high percentage of near-contact edges in a thermal network constructed from irregular particles such as crushed Schist results in a high $[G^T]_{C_{n1}}$ [28]. As heat transfer is lower through near-contacts than that in interparticle contacts, thermal conductance was added as weight at thermal network edges to obtain $[G^T]_{C_{nw2}}$ (Feature 13). A near-contact acting as the shortest path in the unweighted thermal network may not be the shortest path in the weighted thermal network since thermal conductance is low at near-contacts. Fig. 11(b) shows the increase in $[G^C]_{C_{nw1}}$ with ETC, which is similar to the effect of $[G^C]_{\kappa_w}$ on ETC, as shown in Fig. 10(b). Since Fig. 9 shows $[G^*]_{C_{nw2}}$ (Feature 13) from both contact network and thermal network have high linear correlation (R^2 around 0.95) with ETC, the relationships are plotted in Fig. 11(c) for $[G^C]_{C_{nw2}}$ and Fig. 11(d) for $[G^T]_{C_{nw2}}$, respectively. The relationship between $[G^T]_{C_{nw2}}$ and ETC is described by Equation 7, this simple linear equation results in a similar R^2 as the Quadratic polynomial Equation 6 which considers $[G^T]_{\kappa_w}$ as a single variable. However, the values of $[G^T]_{C_{nw2}}$ for different sands are not distribute as evenly as the values of $[G^T]_{\kappa_w}$.

<Fig. 11 around here>

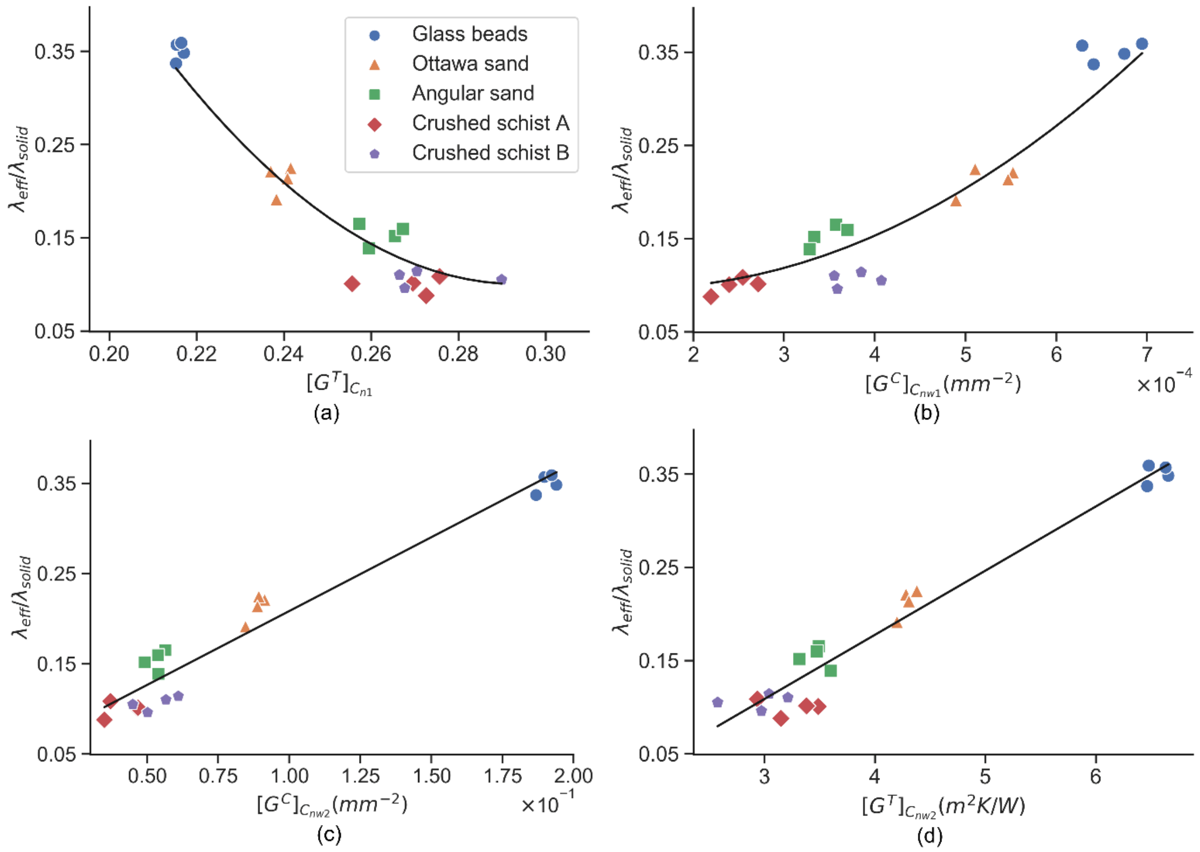

Fig. 11. The relationship between ETC and contact network feature (a) $[G^T]_{C_{n1}}$(*closeness centrality normalised by |V|-1)* and (b) $[G^T]_{C_{nw1}}$ (*weighted closeness centrality normalised by |V|-1)*.

$$\frac{\lambda_{eff}}{\lambda_{solid}} = 0.069[G^T]_{C_{nw1}} - 0.098 \qquad (7)$$

Betweenness centrality is another type of centrality to quantify the importance of a node or edge as a 'bridge'. Fig. 9 shows that contact network features $[G^C]_{B_n^{edge}}$ (Feature 19) and $[G^C]_{B_{nw}^{edge}}$ (Feature 21) have scores larger than 0.9, and their relationships with ETC are shown in Fig. 12. Higher $[G^C]_{B_n^{edge}}$ means that the different parts of the sample are more separated, and ETC is lower in a sample with a larger $[G^C]_{B_n^{edge}}$, as shown in Fig. 12. Since the *betweenness centrality* calculates a percentage (Equation 3) of the shortest path via a node or edge, adding weight keeps the value of the *betweenness centrality* (percentage) within a similar range, even though the shortest paths are changed. The *weighted* *edge betweenness centrality* $[G^C]_{B_{nw}^{edge}}$ also enables data from the a given material to be closer by comparing the data for the angular sand in Fig. 12(a) and Fig. 12Fig. 12(b). In contrast to the *weighted edge betweenness centrality* for the contact network $[G^C]_{B_{nw}^{edge}}$, the *weighted edge betweenness centrality* $[G^T]_{B_{nw}^{edge}}$ for the thermal network has a lower score of 0.78 (Fig. 9). The lower score of $[G^T]_{B_{nw}^{edge}}$ indicates that heat transfer via near-contacts reduces the correlation between *edge betweenness centrality* and ETC, it is possibly because the directions of heat transfer at near-contact edges are not considered when calculating the shortest path. The shortest path with highest local thermal conductance without considering the heat transfer orientation may not be the optimal heat transfer path, resulting in the *average weighted shortest path* $[G^{\mathrm{T}}]_{P_w}$ (Feature 29) in the thermal network having a lower correlation with ETC than $[G^C]_{P_w}$. In contrast, $[G^T]_{B_w^{edge^{tp}}}$ (Feature 22), which only measures the *edge betweenness centrality* in the main heat transfer direction (between the top and bottom sample surfaces) for the thermal network, has a similar score to $[G^C]_{B_w^{edge^{tp}}}$ for the contact network.

<Fig. 12 around here>

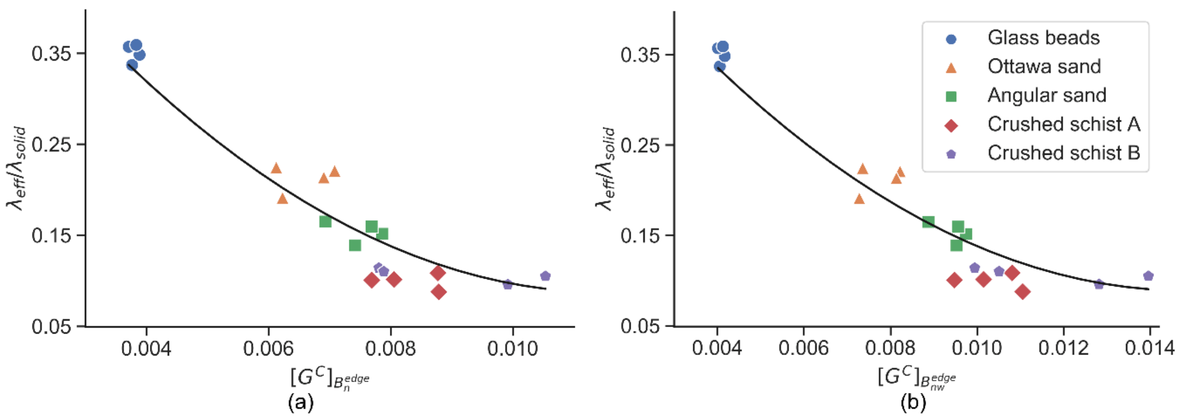

Fig. 12. Contact network features: (a) $[G^C]_{B_n^{edge}}$ (*normalised edge betweenness centrality*) and (b) $[G^C]_{B_{nw}^{edge}}$ (*normalised weighted edge betweenness centrality*) has a high correlation with ETC.

From the definitions of cluster-type and cycle-type features, they are related only to the particle connectivity, without quantifying the contact quality. However, the *local clustering coefficient* $[G^T]_{LC}$

(Feature 32) for the thermal network and the number of *3-cycles* G_{3C}^{C} (Feature 33) for the contact network show good correlation with ETC. Since $[G^T]_{LC}$ measures the density of triangles in the thermal network, ETC decreases with increasing $[G^T]_{LC}$ (Fig. 13(a)) due to the large percentage of near-contacts in irregular particle packings. In contrast, ETC increases with the number of *3-cycles* in regular particle packings, as shown in Fig. 13(b).

<Fig. 13 around here>

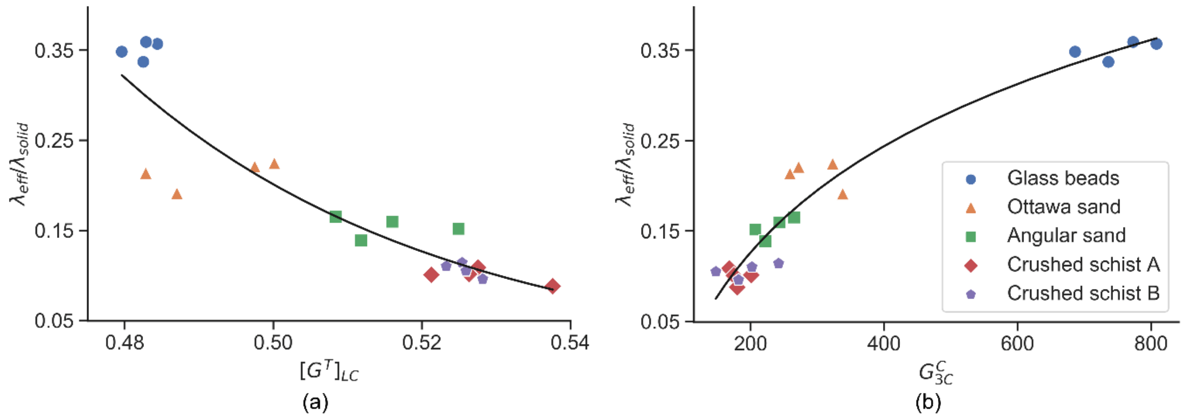

Fig. 13. (a) Thermal network feature $[G^T]_{LC}$ (*local clustering coefficient)* and (b) contact network feature G_{3C}^{C} (*number of 3-cycles*) show good correlation with ETC.

4.3 Relationships between features

Several network features affect ETC and all of these are mesoscale features used to indicate the connectivity of particles, and some consider contact quality. Hence, strong relationships may exist between them. Fig. 9 shows that thermal network features present lower correlations with ETC than contact network features, indicating that correlation between the former is weaker than for the latter. The correlations between each pair of the variables in Table 2 were therefore calculated (network features computed from thermal networks). The same procedures for model selection and feature importance were used to study the relationship between each feature and ETC. Fig. 14 shows that the correlation between centrality features (Features 6–25) is high, and the correlation coefficient between $[G^T]_{\kappa_w}$ (Featrue 7) and $[G^T]_{C_{nw2}}$ (Featrue 13) is 0.94. Fig. 15(a) shows they have a positive relationship since they both measure the weighted particle connectivity. $[G^T]_{B_w^{edge^{tp}}}$ (Feature 22) and $[G^T]_{LC}$

(Feature 32) are both percentages according to their definitions and have a correlation coefficient of 0.80. Fig. 15(b) shows they have a negative relationship, since higher $[G^T]_{B_w^{edge^{tp}}}$ means that a network is more fractured (the sample is looser), while higher $[G^T]_{LC}$ indicates more integration (the sample is denser).

<Fig. 14 around here>

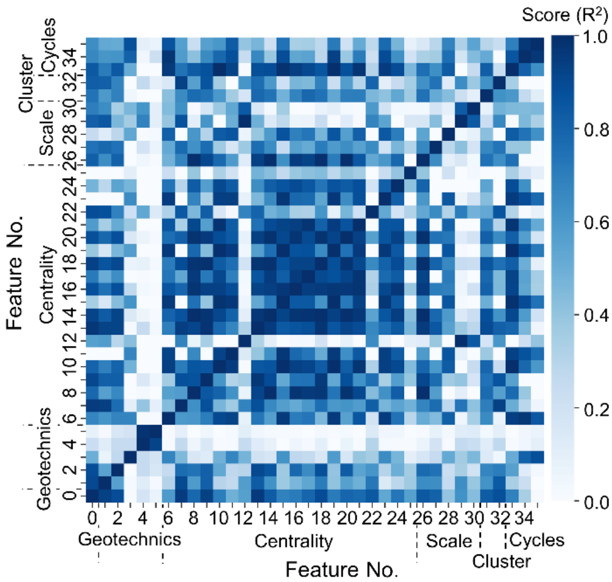

Fig. 14. The score between each two features. Feature 0 is the dimensionless ETC and other features refer to Table 2.

<Fig. 15 around here>

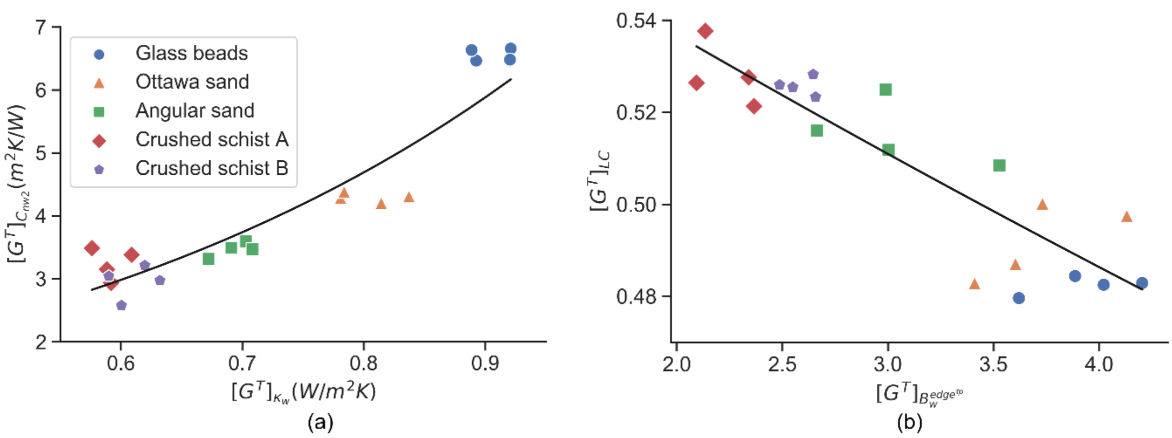

Fig. 15. Relationships between thermal network features: (a) relationship between $[G^T]_{\kappa W}$ (*weighted degree*) and $[G^T]_{C_{n1}}$ (*closeness centrality normalised by* |*V*|-*1*); (b) relationship between $[G^T]_{B_w^{edge}{}^{tp}}$ (*average weighted top-to-bottom edge betweenness centrality*) and $[G^T]_{LC}$ (*local clustering coefficient*).

5. Conclusion

In order to find microstructural features to predict ETC, five sands were selected, and multiple network features for both contact and thermal networks were calculated. After analysing the relationships between each feature and the ETC, network features such as *weighted degree* and *weighted closeness centrality* are good predictors of ETC not only for sphere packings [30] but also for real sands. Their merit is because they can capture more information (both the particle connectivity and contact quality) than traditional parameters such as porosity. The importance of network features to ETC also relieve the concern that the lack of structural data may result in the difference of ETC between models and methods [6]. We also note that estimating ETC accurately using finite element methods may be practically feasible only when enough computational power and higher CT image resolutions are available.

Both contact and thermal network features have certain benefits and limitations. The thin wedge of interstitial gas between two particles [74], moisture content around the interparticle spaces and thermal radiation may enable more indirect heat transfers via ‘near-contacts’, therefore enhance the importance of thermal network features. Some network features may have close correlations with each other, and it may be sufficient to use just one of these in the model.

The acquirement of network features for real sands needs image processing techniques and network construction and feature extractions (i.e. additional mathematic calculations). However, with the affordability of CT and a well-developed framework that the authors are working on, numerous parameters/features can be achieved more efficiently and cost-effectively. For example, twenty-four hours saturation is required to measure the porosity of a sample while it takes thirty minutes CT scanning and five minutes to achieve not only porosity but particle size, shape, connectivity with this framework. Moreover, the work also shows the potential capability of extracting macroscopic quantities related to mechanical response, fluid flow, heat transfer and electrical conduction based on the CT images.

Declaration of Competing Interest

The authors declare that they have no known competing financial interests or personal relationships that could have appeared to influence the work reported in this paper.

Acknowledgements

The authors would like to thank Yu Zhou for photographing the sands, and Dr Anton Maksimenko and the other academics at Australian Synchrotron, Victoria, Australia for supporting us in obtaining images via CT imaging and medical beamline (IMBL). The first author would like to thank the University of Melbourne for support via a Melbourne Research Scholarship and Dr Joost van der Linden and Dr Mahdi Miri Disfani for fruitful discussions.

References

[1] Johnston IW, Narsilio GA, Colls S. Emerging geothermal energy technologies. KSCE Journal of Civil Engineering. 2011;15(4):643-53.
[2] Loveridge F, Holmes G, Powrie W, Roberts T. Thermal response testing through the Chalk aquifer in London, UK. ICE Themes Geothermal Energy, Heat Exchange Systems and Energy Piles2018. p. 157-77.
[3] Xinbao Y, Nan Z, Asheesh P, J. PA. Thermal conductivity of sand–kaolin clay mixtures. Environmental Geotechnics. 2016;3(4):190-202.
[4] Rotta Loria AF, Laloui L. The equivalent pier method for energy pile groups. Géotechnique. 2017;67(8):691-702.
[5] Bidarmaghz A, Choudhary R, Soga K, Kessler H, Terrington RL, Thorpe S. Influence of geology and hydrogeology on heat rejection from residential basements in urban areas. Tunnelling and Underground Space Technology. 2019;92(103068.
[6] Yüksel N. The review of some commonly used methods and techniques to measure the thermal conductivity of insulation materials. Insulation Materials in Context of Sustainability: IntechOpen, 2016.
[7] Yun TS, Santamarina JC. Fundamental study of thermal conduction in dry soils. Granular matter. 2008;10(3):197-207.
[8] Dong Y, McCartney JS, Lu N. Critical Review of Thermal Conductivity Models for Unsaturated Soils. Geotechnical and Geological Engineering. 2015;33(2):207-21.
[9] Zhang N, Wang Z. Review of soil thermal conductivity and predictive models. International Journal of Thermal Sciences. 2017;117(172-83.
[10] Chu Z, Zhou G, Wang Y, Zhao X, Mo P-Q. A supplementary analytical model for the stagnant effective thermal conductivity of low porosity granular geomaterials. International Journal of Heat and Mass Transfer. 2019;133(994-1007.
[11] Abdulagatova Z, Abdulagatov I, Emirov V. Effect of temperature and pressure on the thermal conductivity of sandstone. International Journal of Rock Mechanics and Mining Sciences. 2009;46(6):1055-71.
[12] Mo J, Ban H. Measurements and theoretical modeling of effective thermal conductivity of particle beds under compression in air and vacuum. Case studies in thermal engineering. 2017;10(423-33.
[13] Batchelor GK, O'brien R. Thermal or electrical conduction through a granular material. Proc R Soc Lond A. 1977;355(1682):313-33.

[14] Dai W, Hanaor D, Gan Y. The effects of packing structure on the effective thermal conductivity of granular media: A grain scale investigation. International Journal of Thermal Sciences. 2019;142(266-79.
[15] Finney J. Random packings and the structure of simple liquids. I. The geometry of random close packing. Proc R Soc Lond A. 1970;319(1539):479-93.
[16] Cheng G, Yu A, Zulli P. Evaluation of effective thermal conductivity from the structure of a packed bed. Chemical Engineering Science. 1999;54(19):4199-209.
[17] Bahrami M, Culham J, Yovanovich M. Modeling thermal contact resistance: a scale analysis approach. Journal of heat transfer. 2004;126(6):896-905.
[18] Liang Y. Expression for effective thermal conductivity of randomly packed granular material. International Journal of Heat and Mass Transfer. 2015;90(1105-8.
[19] Siu W, Lee S-K. Effective conductivity computation of a packed bed using constriction resistance and contact angle effects. International journal of heat and mass transfer. 2000;43(21):3917-24.
[20] Torquato S, Haslach Jr H. Random heterogeneous materials: microstructure and macroscopic properties. Appl Mech Rev. 2002;55(4):B62-B3.
[21] Nadimi S, Fonseca J, Andò E, Viggiani G. A micro finite-element model for soil behaviour: experimental evaluation for sand under triaxial compression. Géotechnique. 2019;0(0):1-6.
[22] Reimann J, Vicente J, Brun E, Ferrero C, Gan Y, Rack A. X-ray tomography investigations of mono-sized sphere packing structures in cylindrical containers. Powder technology. 2017;318(471-83.
[23] Druckrey A, Alshibli K, Al-Raoush R. Discrete particle translation gradient concept to expose strain localisation in sheared granular materials using 3D experimental kinematic measurements. Géotechnique. 2017;68(2):162-70.
[24] Tordesillas A, Tobin ST, Cil M, Alshibli K, Behringer RP. Network flow model of force transmission in unbonded and bonded granular media. Physical Review E. 2015;91(6):062204.
[25] Sufian A, Russell AR, Whittle AJ. Anisotropy of contact networks in granular media and its influence on mobilised internal friction. Géotechnique. 2017;67(12):1067-80.
[26] Papadopoulos L, Porter MA, Daniels KE, Bassett DS. Network analysis of particles and grains. Journal of Complex Networks. 2018;6(4):485-565.
[27] Russell S, Walker DM, Tordesillas A. A characterization of the coupled evolution of grain fabric and pore space using complex networks: Pore connectivity and optimized flows in the presence of shear bands. Journal of the Mechanics and Physics of Solids. 2016;88(227-51.
[28] Fei W, Narsilio GA, van der Linden JH, Disfani MM. Quantifying the impact of rigid interparticle structures on heat transfer in granular materials using networks. International Journal of Heat and Mass Transfer. 2019;143(118514.
[29] Fei W, Narsilio GA, Disfani MM. Impact of three-dimensional sphericity and roundness on heat transfer in granular materials. Powder Technology. 2019;355(770-81.
[30] Fei W, Narsilio GA, van der Linden JH, Disfani MM. Network analysis of heat transfer in sphere packings. Powder Technology. 2020;362(790-804.
[31] Alramahi B, Alshibli KA, Fratta D. Effect of Fine Particle Migration on the Small-Strain Stiffness of Unsaturated Soils. Journal of Geotechnical and Geoenvironmental Engineering. 2010;136(4):620-8.
[32] Roshankhah S, Santamarina JC. Engineered granular materials for heat conduction and load transfer in energy geotechnology. Géotechnique Letters. 2014;4(2):145-50.
[33] Yang J, Gu XQ. Shear stiffness of granular material at small strains: does it depend on grain size? Géotechnique. 2013;63(2):165-79.
[34] ASTM. C778-17 standard specification for standard sand. ASTM International, West Conshohocken, PA. 2017.
[35] Zhang N, Yu X, Pradhan A, Puppala AJ. Thermal conductivity of quartz sands by thermo-time domain reflectometry probe and model prediction. Journal of Materials in Civil Engineering. 2015;27(12):04015059.
[36] Neuendorf KK, Mehl Jr JP, Jackson JA. Glossary of Geology: American Geological Institute. Alexandria, Virginia. 2005.
[37] Narsilio GA, Buzzi O, Fityus S, Yun TS, Smith DW. Upscaling of Navier–Stokes equations in porous media: Theoretical, numerical and experimental approach. Computers and Geotechnics. 2009;36(7):1200-6.
[38] Azadi P, Farnood R, Yan N. FEM–DEM modeling of thermal conductivity of porous pigmented coatings. Computational Materials Science. 2010;49(2):392-9.
[39] Łydżba D, Różański A. Microstructure measures and the minimum size of a representative volume element: 2D numerical study. Acta Geophysica. 2014;62(5):1060-86.
[40] Fei W, Narsilio GA. Impact of three-dimensional sphericity and roundness on coordination number. Journal of Geotechnical and Geoenvironmental Engineering. 2020:(Accepted).
[41] Otsu N. A threshold selection method from gray-level histograms. IEEE transactions on systems, man, and cybernetics. 1979;9(1):62-6.

[42] Schlüter S, Sheppard A, Brown K, Wildenschild D. Image processing of multiphase images obtained via X‐ray microtomography: a review. Water Resources Research. 2014;50(4):3615-39.
[43] Karatza Z, Andò E, Papanicolopulos S, Ooi J, Viggiani G. Evolution of deformation and breakage in sand studied using X-ray tomography. Géotechnique. 2018;1(1-11.
[44] Wiebicke M, Andò E, Herle I, Viggiani G. On the metrology of interparticle contacts in sand from x-ray tomography images. Measurement Science and Technology. 2017;28(12):124007.
[45] Yun TS, Santamarina JC. Fundamental study of thermal conduction in dry soils. Granular matter. 2008;10(3):197.
[46] Yun TS, Evans TM. Three-dimensional random network model for thermal conductivity in particulate materials. Computers and Geotechnics. 2010;37(7):991-8.
[47] Sundberg J, Back P-E, Ericsson LO, Wrafter J. Estimation of thermal conductivity and its spatial variability in igneous rocks from in situ density logging. International Journal of Rock Mechanics and Mining Sciences. 2009;46(6):1023-8.
[48] Haigh SK. Thermal conductivity of sands. Géotechnique. 2012;62(7):617-25.
[49] Simpleware Ltd. Simpleware ScanIP, http://www.simpleware.com/software/scanip. Date of access. 2015;15(12.
[50] AB C. COMSOL multiphysics v5.0, http://www.comsol.com. 2015.
[51] Narsilio GA, Kress J, Yun TS. Characterisation of conduction phenomena in soils at the particle-scale: Finite element analyses in conjunction with synthetic 3D imaging. Computers and Geotechnics. 2010;37(7):828-36.
[52] Carslaw H, Jaeger J. Conduction of heat in solids: Oxford Science Publications: Oxford, England, 1959.
[53] ASTM D5334-14. Standard Test Method for Determination of Thermal Conductivity of Soil and Soft Rock by Thermal Needle Probe Procedure. West Conshohocken, PA: ASTM International, 2014.
[54] Brandon T, Mitchell J. Factors influencing thermal resistivity of sands. Journal of Geotechnical Engineering. 1990;115(12):1683-98.
[55] Legland D, Arganda-Carreras I, Andrey P. MorphoLibJ: integrated library and plugins for mathematical morphology with ImageJ. Bioinformatics. 2016;32(22):3532-4.
[56] Schindelin J, Arganda-Carreras I, Frise E, Kaynig V, Longair M, Pietzsch T, et al. Fiji: an open-source platform for biological-image analysis. Nature methods. 2012;9(7):676.
[57] Fonseca J, O'Sullivan C, Coop MR, Lee P. Non-invasive characterization of particle morphology of natural sands. Soils and Foundations. 2012;52(4):712-22.
[58] van der Linden JH, Narsillio GA, Antoinette T. Thermal conductance network model for computerised tomography images of real geomaterials (Conditionally accepted). Computers and Geotechnics. 2019.
[59] Newman MEJ. Networks : an introduction: Oxford ; New York : Oxford University Press, 2010., 2010.
[60] Freeman LC. Centrality in social networks conceptual clarification. Social networks. 1978;1(3):215-39.
[61] Freeman LC. A set of measures of centrality based on betweenness. Sociometry. 1977:35-41.
[62] Laman G. On graphs and rigidity of plane skeletal structures. Journal of Engineering mathematics. 1970;4(4):331-40.
[63] Asimow L, Roth B. The rigidity of graphs. Transactions of the American Mathematical Society. 1978;245(279-89.
[64] Crapo H. Structural rigidity. Structural topology, 1979, núm 1. 1979.
[65] Tordesillas A, Lin Q, Zhang J, Behringer R, Shi J. Structural stability and jamming of self-organized cluster conformations in dense granular materials. Journal of the Mechanics and Physics of Solids. 2011;59(2):265-96.
[66] Newman ME. The structure and function of complex networks. SIAM review. 2003;45(2):167-256.
[67] Watts DJ, Strogatz SH. Collective dynamics of 'small-world'networks. nature. 1998;393(6684):440.
[68] Abyzov AM, Goryunov AV, Shakhov FM. Effective thermal conductivity of disperse materials. I. Compliance of common models with experimental data. International Journal of Heat and Mass Transfer. 2013;67(752-67.
[69] Liu F, Cai Y, Wang L, Zhao J. Effects of nanoparticle shapes on laminar forced convective heat transfer in curved ducts using two-phase model. International Journal of Heat and Mass Transfer. 2018;116(292-305.
[70] van der Linden JH, Narsilio GA, Tordesillas A. Machine learning framework for analysis of transport through complex networks in porous, granular media: a focus on permeability. Physical Review E. 2016;94(2):022904.
[71] Santosa F, Symes WW. Linear inversion of band-limited reflection seismograms. SIAM Journal on Scientific and Statistical Computing. 1986;7(4):1307-30.
[72] Pedregosa F, Varoquaux G, Gramfort A, Michel V, Thirion B, Grisel O, et al. Scikit-learn: Machine learning in Python. Journal of machine learning research. 2011;12(Oct):2825-30.
[73] Stone M. Cross-validatory choice and assessment of statistical predictions. Journal of the royal statistical society Series B (Methodological). 1974:111-47.
[74] Morris AB, Pannala S, Ma Z, Hrenya CM. A conductive heat transfer model for particle flows over immersed surfaces. International Journal of Heat and Mass Transfer. 2015;89(1277-89.

Appendix

Appendix 1 The score and model used to evaluate the importance of each feature to ETC.

Type	NO.	Notation	Contact network features		Thermal network features	
			Score	Model	Score	Model
Geotechnics	1	n	0.9317	Quadratic polynomial	0.9317	Quadratic polynomial
	2	γ	0.8889	Linear	0.8889	Linear
	3	D_{50}	0.0106	Cubic Polynomial	0.0106	Cubic Polynomial
	4	C_u	0.1772	Logarithmic	0.1772	Logarithmic
	5	C_c	0.0694	Logarithmic	0.0694	Logarithmic
Centrality	6	$[G^*]_\kappa$	0.9638	Linear	0.5883	Cubic Polynomial
	7	$[G^*]_{\kappa_w}$	0.9184	Quadratic polynomial	0.9515	Quadratic polynomial
	8	$[\mathrm{G}^*]_\mathrm{C}$	0.7084	Logarithmic	0.783	Logarithmic
	9	$[\mathrm{G}^*]_{\mathrm{C}_{\mathrm{n1}}}$	0.7129	Cubic Polynomial	0.9354	Quadratic polynomial
	10	$[G^*]_{C_{n2}}$	0.8281	Linear	0.7055	Cubic Polynomial
	11	$[G^*]_{C_w}$	0.1831	Quadratic polynomial	0.4884	Cubic Polynomial
	12	$[G^*]_{C_{nw1}}$	0.914	Quadratic polynomial	0.5629	Power
	13	$[G^*]_{C_{nw2}}$	0.9481	Linear	0.9545	Linear
	14	$[G^*]_{B^{node}}$	0.7539	Linear	0.8352	Linear
	15	$[G^*]_{B_n^{node}}$	0.8336	Quadratic polynomial	0.691	Cubic Polynomial
	16	$[G^*]_{B_w^{node}}$	0.6613	Linear	0.7129	Linear
	17	$[G^*]_{B_{nw}^{node}}$	0.8818	Quadratic polynomial	0.7961	Cubic Polynomial
	18	$[G^*]_{B^{edge}}$	0.6148	Cubic Polynomial	0.8924	Linear
	19	$[G^*]_{B_n^{edge}}$	0.9207	Quadratic polynomial	0.7119	Cubic Polynomial
	20	$[G^*]_{B_w^{edge}}$	0.3219	Cubic Polynomial	0.7963	Linear
	21	$[G^*]_{B_{nw}^{edge}}$	0.9356	Quadratic polynomial	0.7754	Cubic Polynomial
	22	$[G^*]_{B_w^{edge^{tp}}}$	0.8232	Quadratic polynomial	0.8416	Exponential
	23	$[G^*]_{B_{nw}^{edge^{tp}}}$	0.5777	Logarithmic	0.5318	Cubic Polynomial
	24	$[G^*]_E$	0.2557	Logarithmic	0.7287	Cubic Polynomial
	25	$[G^*]_{E_w}$	0.7846	Quadratic polynomial	0.5632	Quadratic polynomial
Network scale	26	G_ρ^*	0.5631	Cubic Polynomial	0.8434	Quadratic polynomial
	27	G_D^*	0.1922	Linear	0.8051	Quadratic polynomial
	28	$G_{D_n}^*$	0.8627	Quadratic polynomial	0.4004	Cubic Polynomial
	29	$[G^*]_{P_w}$	0.9036	Cubic Polynomial	0.625	Exponential
	30	$[G^*]_{P_w^{tp}}$	0.868	Cubic Polynomial	0.4311	Exponential
Clustering	31	${G^*}_{GC}$	0.7292	Quadratic polynomial	0.8314	Quadratic polynomial
	32	$[G^*]_{LC}$	0.4897	Linear	0.8812	Exponential
Cycles	33	G_{3C}^*	0.9418	Logarithmic	0.688	Quadratic polynomial
	34	$[G^*]_{3C^{node}}$	0.9169	Linear	0.344	Cubic Polynomial
	35	$[G^*]_{3C^{\mathrm{edge}}}$	0.8401	Quadratic polynomial	0.0121	Logarithmic

[G]* is a unified characteristic, and *[G^C]* refers to *contact* network features, while *[G^T]* refers to *thermal* networks. The brackets in *[G*]* indicate an average value of the parameter.

List of Figures

Fig. 1. Five types of natural sand scanned with computed tomography.

Fig. 2 Framework used to calculate the microstructural parameters and analyse their impact on the effective thermal conductivity of granular materials.

Fig. 3 The process of heat transfer simulation based on CT scanned images.

Fig. 4 The heat transfer path includes both interparticle contact and the small gaps between particles. Only interparticle contact is considered in the *contact* network, while both paths are involved in the *thermal* network.

Fig. 5 Identification of the interparticle contact and the near-contact in (a) a sphere packing and (b) a real sand from voxelated images.

Fig. 6. Network features: (a) The highest values of the different types of centrality features are found for different nodes in a given network,; (b) Network scale features and (c) Clustering coefficients [30].

Fig. 7. The ETC of five types of sand are computed using the finite element method and validated using experimental results.

Fig. 8. Contact and thermal networks: (a) Only real contacts (red edges) are considered in a contact network, while (b) both real contacts and 'near-contacts' (blue edges) are considered in a thermal network for the same sample. Sand grains were presented by spheres with equivalent particle diameter.

Fig. 9. The importance of each feature to ETC (feature number refers to the listing in Table 2).

Fig. 10. Relationship between ETC and (a) contact network feature *degree* $[G^C]_\kappa$ (coordination number); (b) contact network feature *weighted degree* $[G^C]_{\kappa_W}$; (c) : *contact radius ratio* γ; and (d) thermal network feature *weighted degree* $[G^T]_{\kappa_W}$.

Fig. 11. The relationship between ETC and contact network feature (a) $[G^T]_{C_{n1}}$ (*closeness centrality normalised by* |*V*|-*1)* and (b) $[G^T]_{C_{nw1}}$ (*weighted closeness centrality normalised by* |*V*|-*1).*

Fig. 12. Contact network features: (a) $[G^C]_{B_n^{edge}}$ (*normalised edge betweenness centrality*) and (b) $[G^C]_{B_{nw}^{edge}}$ (*normalised weighted edge betweenness centrality*) has a high correlation with ETC.

Fig. 13. (a) Thermal network feature $[G^T]_{LC}$ (*local clustering coefficient)* and (b) contact network feature G_{3C}^C (*number of 3-cycles*) show good correlation with ETC.

Fig. 14. The score between each two features. Feature 0 is the dimensionless ETC and other features refer to Table 2.

Fig. 15. Relationships between thermal network features: (a) relationship between $[G^T]_{\kappa_W}$ (*weighted degree*) and $[G^T]_{C_{n1}}$ (*closeness centrality normalised by* |*V*|-*1*); (b) relationship between $[G^T]_{B_w^{edge^{tp}}}$ (*average weighted top-to-bottom edge betweenness centrality*) and $[G^T]_{LC}$ (*local clustering coefficient*).

List of Tables

Table 1 Particle size for the selected sands
Table 2 Summary of features used in this work